CRYSTAL GROWTH & DESIGN

pubs.acs.org/crystal

Article

Integration of Self-Assembled $BaZrO_3$-Co Vertically Aligned Nanocomposites on Mica Substrates toward Flexible Spintronics

Juncheng Liu, Xuejing Wang, Xingyao Gao, Han Wang, Bruce Zhang, Di Zhang, Matias Kalaswad, Jijie Huang, and Haiyan Wang*

Cite This: *Cryst. Growth Des.* 2022, 22, 718−725

Read Online

ACCESS | Metrics & More | Article Recommendations | Supporting Information

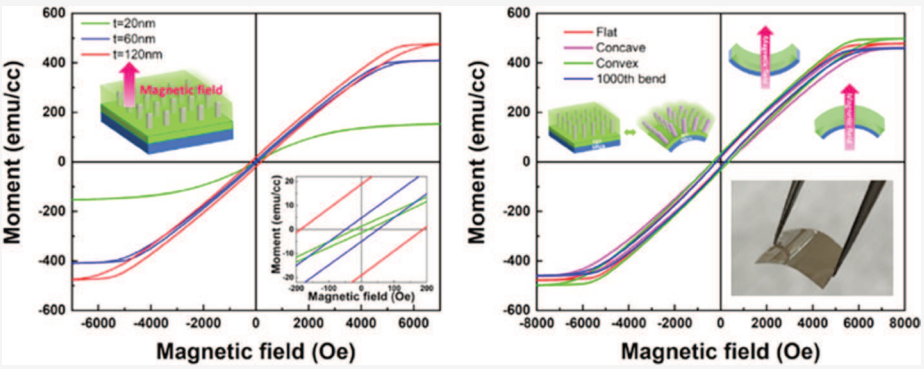

ABSTRACT: Integrating functional thin films with anisotropic physical properties onto flexible substrates is of great interest for future flexible electronic applications. In this work, self-assembled $BaZrO_3$(BZO)-Co vertically aligned nanocomposite thin films have been integrated onto flexible mica substrates using pulsed laser deposition. Microstructure characterization shows high-quality growth of Co nanopillars in the BZO matrix. Tunable, anisotropic ferromagnetic properties of the films have been achieved by controlling the film thickness and the aspect ratio of Co nanopillars. The bending stability tests have been carried out under different bending conditions and cyclic bending conditions to explore the physical property variation of the films. The successful integration of BZO-Co on mica substrates opens a way for future flexible spintronics and device integration.

INTRODUCTION

Driven by the needs of wearable, flexible devices and the demands for next-generation electronics, tremendous efforts have been put forward on integrating functional materials on flexible substrates.[1−6] These integrated functional thin films have great potentials in applications such as flexible displays, lightweight wearable electronics, and intelligent sensors.[7−9] Typically, there are two approaches to achieve thin-film integration on flexible substrates. One way is depositing thin films on metal foils, which needs careful surface treatment of the metal substrates.[10−12] In addition to the metallic flexible substrates, muscovite mica is known to be a suitable flexible platform for thin-film deposition. It is biocompatible, with high thermal stability, lightweight, and low cost, and several studies have been demonstrated on integrating functional thin films with these mica substrates.[13−21] The second approach is via wafer transfer, which is first depositing the film on a rigid substrate and followed by film transferring onto a flexible polymer.[22] This is an effective approach for flexible polymer substrates, which cannot withstand high-temperature depositions. However, this method requires multiple steps and the wafer-transfer process is challenging.

Multifunctional nanocomposite thin films that integrate electrical, optical, and/or magnetic properties are of great interest and have led to new physical properties and new device concepts.[23] As a unique class of nanocomposite thin films, vertically aligned nanocomposite (VAN) is a self-assembled nanocomposite system with one phase vertically embedded in another phase. It is a new platform that presents enormous opportunities in functional thin-film designs with novel physical properties and strong anisotropy. Previous VAN demonstrations are mostly oxide−oxide ones[24−28] with several recent demonstrations on oxide−metal VANs.[29−33] In these oxide−metal VANs, the morphology of the metal phase and their physical properties are easily tuned by controlling the deposition parameters, which leads to tailored physical properties and various device applications.[34−38] One such

Received: October 20, 2021
Revised: December 6, 2021
Published: December 20, 2021

https://doi.org/10.1021/acs.cgd.1c01227
Cryst. Growth Des. 2022, 22, 718−725

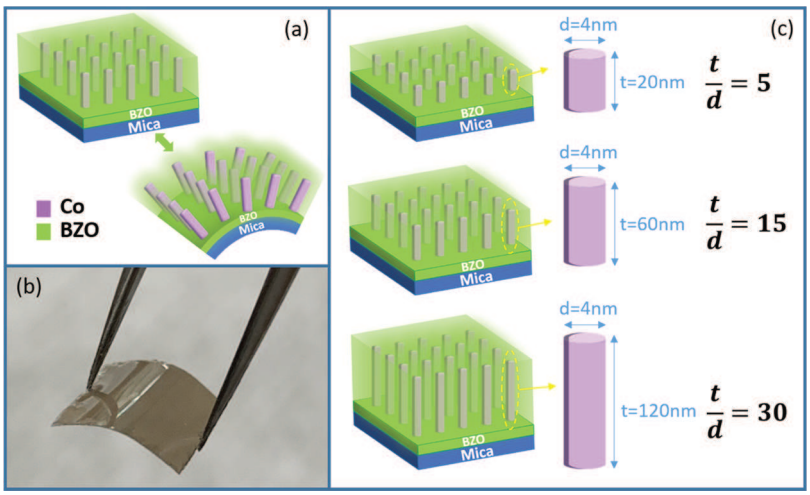

Figure 1. (a) Schematic drawing of a bendable BZO-Co film, (b) photo of the BZO-Co film when bent convexly, and (c) schematic drawing of the BZO-Co film with different thicknesses and different aspect ratios of Co pillars.

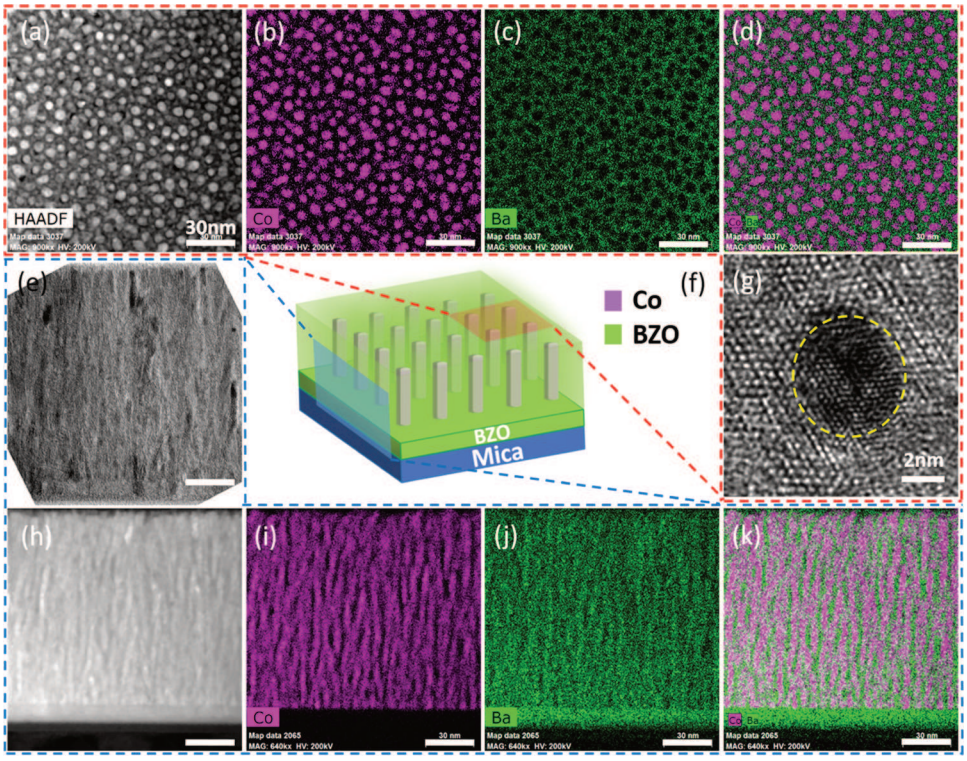

Figure 2. (a) Plan-view high-angle annular dark-field (HAADF) STEM image of the film, with (b–d) corresponding EDS images; (e) cross-sectional TEM image of the film; (f) schematic drawing of the film; (g) plan-view high-resolution TEM (HRTEM) image of the film; and (h) cross-sectional STEM image of the film, with (i–k) corresponding EDS images. (a–e), (h–k) have the same scale bar.

application, spintronics, has device potential as magnetic sensors, spin-torque oscillator, magnetoresistive random-access memory (MRAM), etc.[39−45] Among the materials for spintronics, ferromagnetic metallic nanostructures, including Fe, Co, and Ni, are one of the key components for spintronic devices. Most of the spintronic devices and components have been integrated on single-crystal oxide substrates, such as $SrTiO_3$ and MgO,[25,27,30,31,34,35] with limited reports on single-crystalline Si substrates[46] or flexible mica substrates. For those demonstrated on flexible mica substrates, they are mostly single-phase oxide or oxide−oxide nanocomposites, such as $CaVO_3$, $La_{0.7}Sr_{0.3}MnO_3$ (LSMO):NiO, $BiFeO_3$:$CoFe_2O_4$, etc.[19,21,47] The demonstrations of oxide−metal VAN systems on mica are very scarce,[20] largely due to the growth challenges in achieving van der Waals epitaxy between VAN and mica.

In this work, we successfully integrated a self-assembled $BaZrO_3$(BZO)-Co oxide−metal VAN structure on a mica substrate toward spintronic applications. This system has been previously grown on single-crystalline $SrTiO_3$(STO) substrates using a pulsed laser deposition (PLD) method.[30,34] Here, Co is selected because of its excellent ferromagnetic property, while BZO is selected because of its high chemical and physical stability. A thin ∼10 nm BZO buffer layer was first grown to facilitate the van der Waals epitaxy of the BZO-Co film on

https://doi.org/10.1021/acs.cgd.1c01227
Cryst. Growth Des. 2022, 22, 718−725

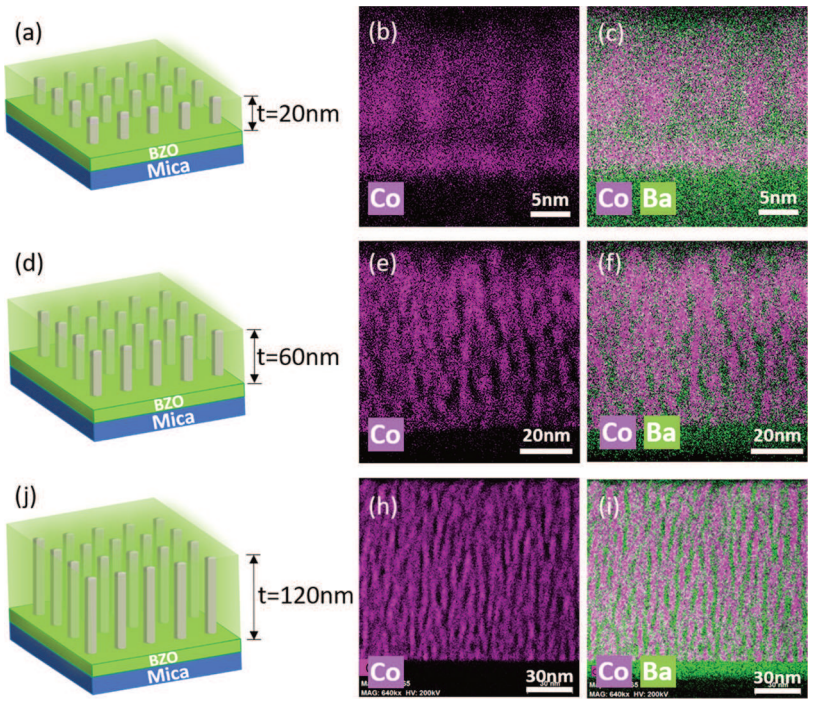

Figure 3. (a, d, f) Schematic drawings of the BZO-Co film with the different thicknesses, with corresponding EDS mapping of (b, e, h) Co and (c, f, i) Co/Ba.

mica, as shown in the schematic drawing in Figure 1a,c. Different thicknesses of the BZO-Co films are proposed to achieve tunable magnetic anisotropy, considering the aspect ratio tuning in the magnetic Co nanopillars. To examine the stability of the VAN films on mica, the films were bent concavely and convexly as well as underwent a cyclic bending test, as the photo in Figure 1b shows one such sample bent convexly. Magnetic and optical properties of the samples before and after the bending test were measured and compared to demonstrate the potentials of these oxide−metal VANs on flexible mica substrates.

RESULTS AND DISCUSSION

Microstructure characterizations, including transmission electron microscopy (TEM), scanning transmission electron microscopy (STEM), and electron dispersive X-ray spectroscopy (EDS) analysis, were performed to explore the morphology of the BZO-Co films grown on mica. Figure 2 shows a summary of the microstructure characterization images of the film with a thickness of 120 nm. Figure 2a shows a low-magnification plan-view STEM image of the film, with the corresponding EDS mapping results shown in Figure 2b−d for Co, Ba, and Co/Ba, respectively. The round shape of Co pillars is confirmed where BZO is the matrix. The [0002] textured Co pillars and the [110] textured BZO matrix were determined based on the high-resolution plan-view TEM image, as shown in Figure 2g. The estimated average diameter of the Co pillars is around 4 nm. The EDS mapping images of films with three different thicknesses are shown in Figure 3. It is clear that all three films present vertically aligned Co pillars grown in the BZO matrix based on the EDS mapping results.

To further explore the crystallinity of the films, X-ray diffraction (XRD) analysis was conducted, and the results are plotted in Figure S1. Typically, a similar crystal structure and lattice parameters are required for the epitaxial growth of thin films. In this work, because of the nature of van der Waals epitaxy, the crystal structure as well as lattice parameters of the mica substrate (monoclinic, a = 0.517 nm, b = 0.894 nm, c = 2.001 nm) are quite different from those of BZO (cubic, a = 0.4193 nm) and Co (hexagonal close-packed (HCP), a = 0.2503nm, c = 0.4061 nm). All of the films show highly textured growth of BZO (110). The Co (0002) peak (at 2θ = 44.762°) could be overlapped with the mica (005) peak (2θ = 44.996°) since the growth orientation of Co can be defined better based on the previous plan-view HRTEM shown in Figure 2g. The Raman spectra for the 20 nm film and the pure BZO film are plotted in Figure S2, suggesting there is no Co−O bonding within the BZO-Co film, while Co could potentially form Co−Zr bonding at the oxide−metal interface, as such metal−metal bonding interfaces have been reported previously in other oxide−metal VAN systems.[48]

To investigate how the aspect ratio of Co pillars affects the magnetic anisotropy of the films, both in-plane (IP, parallel to the measured surface) and out-of-plane (OP, perpendicular to the measured surface) magnetic responses of the samples with different film thicknesses were measured using VSM in MPMS at 300 K, as shown in Figure 4a,b. The IP magnetic saturation moments (M_s) are 160, 335, and 400 emu/cc, while the OP Ms values are 153, 410, and 475 emu/cc for the 20, 60, and 120 nm films, respectively. In addition, the IP coercive field values are 11, 47, and 94 Oe, while the OP coercive field values are 20, 48, and 186 Oe for the 20, 60, and 120 nm films, respectively. Apparently, both the saturation moment as well as the coercivity of the films increase as the film thickness increases, and the out-of-plane magnetic anisotropy also becomes more obvious. The magnetic results suggest that the tunable magnetic response of a BZO-Co film could be achieved by controlling the film thickness. The results are also consistent with the previous studies, which were demonstrated on $SrTiO_3$ substrates.[30,34]

https://doi.org/10.1021/acs.cgd.1c01227
Cryst. Growth Des. 2022, 22, 718−725

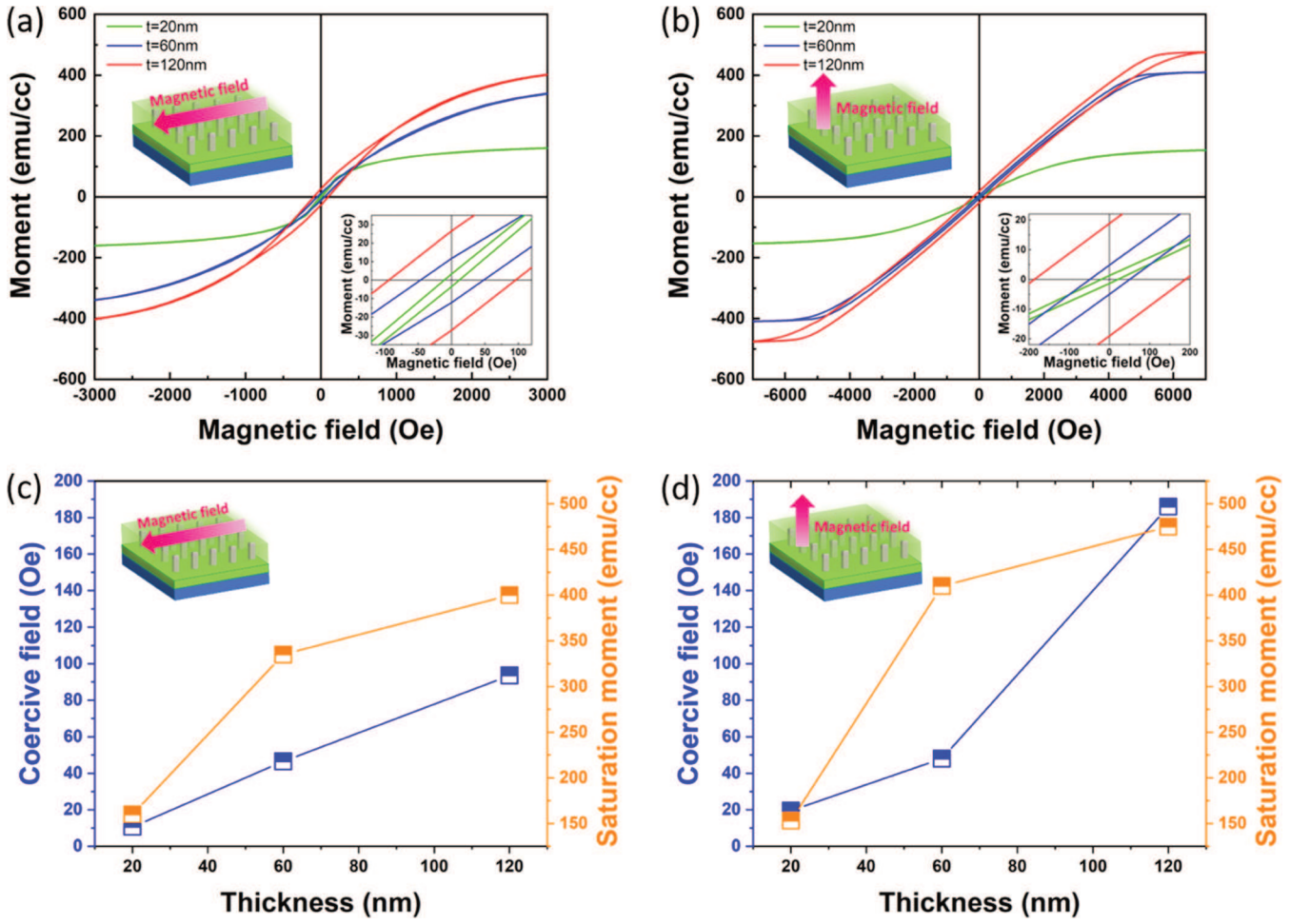

Figure 4. (a) IP and (b) OP $M-H$ curves at room temperature of BZO-Co films with different thicknesses. Summarized (c) in-plane and (d) out-of-plane coercive field and saturation moment of BZO-Co films with different thicknesses.

Considering the VAN integration on flexible mica substrates, it is important to examine the stability of the films against bending. The 120 nm film was selected to measure the IP and OP magnetic properties when bent convexly, concavely, and after 1000th bending at both 300 and 10 K. Before the bending test, the mica substrates were peeled down to around 100 μm to allow the flexible bending. During the bending process, the curvature radius r_c of the samples was around 15 mm. The measured data are plotted in Figure 5. For room-temperature measurement, the IP and OP coercive fields are 96 and 187 Oe, while the IP and OP saturation moments are 425 and 447 emu/cc, respectively. For 10 K measurement, the IP and OP coercive fields are 451 and 1103 Oe, while the IP and OP saturation moments are 519 and 490 emu/cc, respectively. The coercive field and saturation moment for the 120 nm BZO-Co film under different bending conditions and at different temperatures are summarized in Figure 5c,f. The plotted data show a very similar trend for the films at different bending conditions, and no obvious change could be observed for the saturation moment and coercivity. The data suggest very robust and stable magnetic properties of the film against bending, which indicates that the film is promising for future flexible device integration.

It is noted that the M_S values are calculated based on the entire film volume rather than the volume of the Co pillars. Therefore, the magnetization value of Co pillars should be even greater. This is convenient for the property comparison across the different films. Both the saturation moment and the coercive field of the films increase as the film thickness increases, which is due to the elongated magnetic domains. Specifically, the Co pillar length increases as the film grows thicker, and longer Co pillars require a higher applied magnetic field to align, and thus resulting in a higher coercive field. Additionally, it is observed that the coercive field of the films increases significantly when the temperature decreases from room temperature to a low temperature of 10 K, as shown in Figure 5, which is typical for ferromagnetic materials.

Next, optical transmittance measurement was carried out for all three films, as shown in Figure 6a. It is obvious that the intensity of transmittance spectra decreases as the film thickness increases, probably because, as the film thickness increases, the total volume of Co pillars within the film also increases, which would absorb more incident light. As shown in Figure 6b, the transmittance property remained almost unchanged when bent concavely or convexly for the 60 nm film, which suggests a very stable optical transmittance of the nanocomposite film under different bending conditions. Meanwhile, to explore the optical anisotropy of the film introduced by vertical Co pillars, ellipsometry measurements were carried out for the 20 and 120 nm films. The IP ($\varepsilon_{//}$) and OP ($\varepsilon_{\perp}$) dielectric functions of the films were obtained by fitting the ellipsometric parameters Psi (Ψ) and Delta (Δ)

https://doi.org/10.1021/acs.cgd.1c01227
Cryst. Growth Des. 2022, 22, 718−725

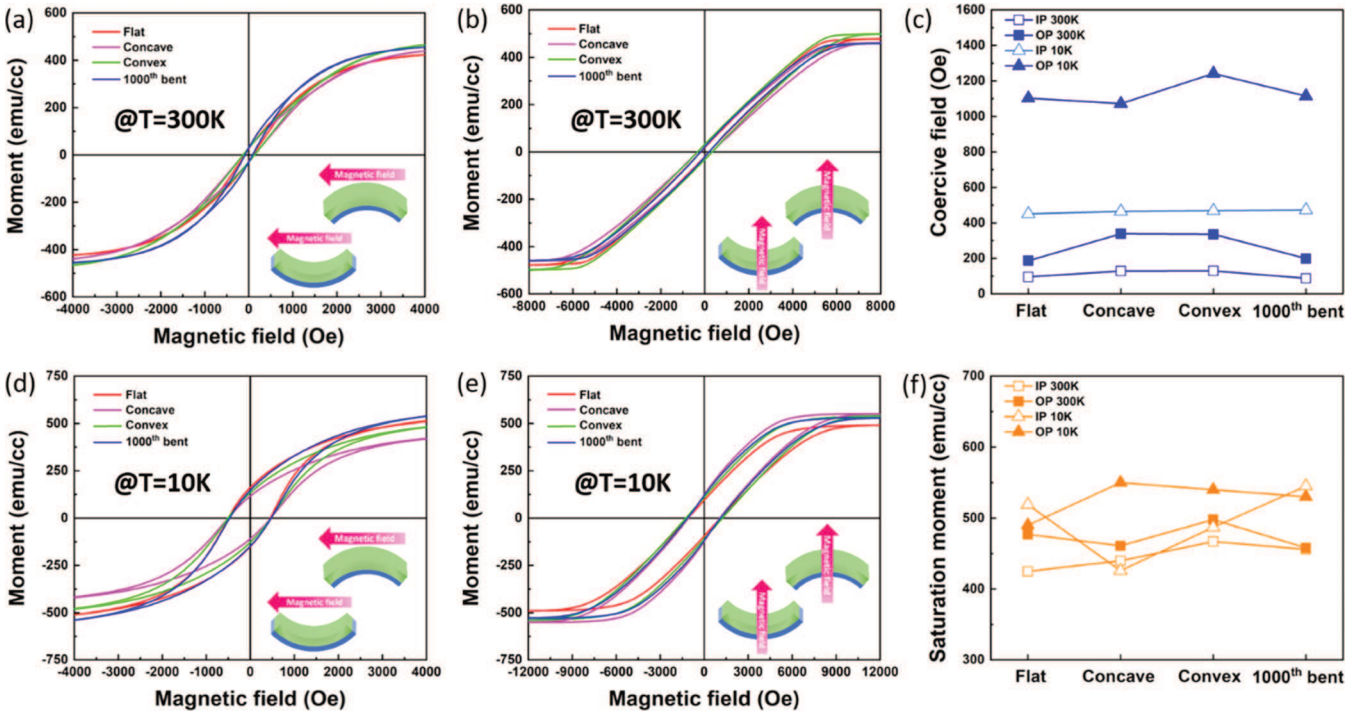

Figure 5. (a) IP and (b) OP $M-H$ curves at room temperature of 120 nm BZO-Co films. (d) IP and (e) OP $M-H$ curves at 10 K of the 120 nm BZO-Co films. Summarized room temperature and 10 K (c) coercive field and (f) saturation moment of the 120 nm BZO-Co films at different bending conditions and after cyclic bending.

using a uniaxial B-spline mode, as shown in Figure 6c,d. The optical anisotropy of the films is confirmed from the obvious difference between the IP and OP real part permittivity for both 20 and 120 nm BZO-Co films; more specifically, the out-of-plane direction is less dielectric ($0 < \varepsilon_{\perp} < \varepsilon_{//}$) for both films, which can be explained by the existence of vertical Co nanopillars within the nanocomposite thin films. A more obvious anisotropy could be observed for the 120 nm film due to the higher aspect ratio of the Co pillars. The imaginary dielectric function of the films is summarized in Figure S2. The positive value of the imaginary permittivity indicates Ohmic losses contributed by metallic Co within the film.[49]

Overall, all films with different thicknesses show high-quality growth of both Co and BZO phases, which ensures the outstanding anisotropic magnetic property of Co and highly stable chemical and physical properties of the BZO matrix. Compared to previous studies on metal–oxide systems on rigid substrates, the film grown on mica in this work has comparable magnetic properties, as well as great advantages due to its flexibility and the potential to be integrated into flexible devices. For future directions, many other oxide–metal VAN systems are worth exploration to be integrated on a mica substrate for flexible spintronics applications beyond BZO-Co, including Fe- and Ni-based oxide–metal VAN systems. Furthermore, the oxide–metal VAN film could be transferred onto a polymer substrate for future flexible device integration. This work demonstrates a crucial step toward the integration of complex multifunctional nanocomposites for flexible spintronics and other electronics.

CONCLUSIONS

In summary, the BZO-Co VAN films have been successfully integrated on flexible mica substrates using a one-step PLD technique. The films show obvious anisotropic magnetic properties owing to their structural anisotropy, i.e., Co nanopillars. Tunable ferromagnetic properties have been achieved by controlling the film thickness and the aspect ratio of Co pillars. The films show very robust physical properties under different bending conditions as well as the cyclic bending test. This work opens an avenue of integrating oxide–metal VAN on mica for future flexible spintronics and electronics integration.

EXPERIMENTAL SECTION

Thin-Film Growth. A solid-state sintering process at 1000 °C was conducted to prepare the BZO-Co (molar ratio 1:1) target. The thin films were deposited using a PLD system with a KrF excimer laser (Lambda Physik Compex Pro 205, λ = 248 nm). The chamber pressure was 2×10^{-6} mTorr during deposition. Laser frequencies of 2 and 5 Hz were used for the BZO buffer layer and the BZO-Co layer deposition. The deposition temperature was kept at 700 °C.

Structural Characterization. XRD (a Panalytical X'Pert X-ray diffractometer) was used to characterize the film crystallinity. TEM, STEM, and EDS (Thermo Fisher Scientific TALOS F200X) were used to characterize the microstructure of the films. A process with grinding and ion milling (PIPS 695, Gatan Inc.) was carried out to make TEM samples. The Raman spectra were measured using a Renishaw's inVia Raman microscope.

Magnetic Property Measurements. A Quantum Design MPMS-3 SQUID Magnetometer was used for magnetic property measurements. The bending process was conducted on a homemade curved holder.

Optical Property Measurements. The transmittance measurements were conducted using a UV–vis–NIR spectrophotometer (Perkin Elmer Lambda 1050). A spectroscopic ellipsometer (J.A. Woollam RC2) was used to conduct ellipsometry measurements.

https://doi.org/10.1021/acs.cgd.1c01227
Cryst. Growth Des. 2022, 22, 718–725

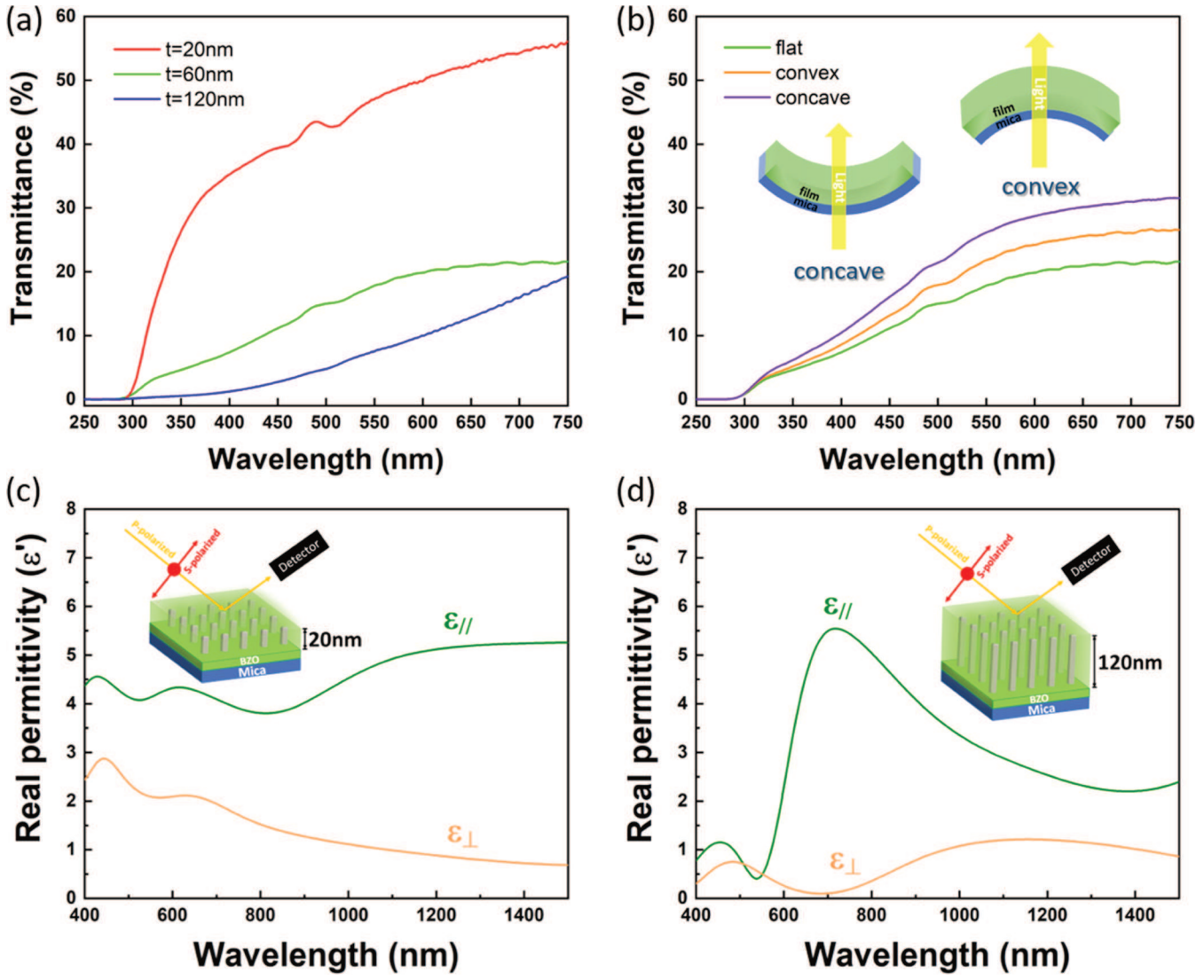

Figure 6. (a) Transmittance results of the BZO-Co films with different thicknesses and (b) transmittance results of the 60 nm BZO-Co film at different bending conditions. Schematic drawings of different bending modes are shown as insets. Real part IP ($\varepsilon_{//}$) and OP ($\varepsilon_{\perp}$) permittivities of the (c) 20 nm and (d) 120 nm BZO-Co films.

■ ASSOCIATED CONTENT

Supporting Information

The Supporting Information is available free of charge at https://pubs.acs.org/doi/10.1021/acs.cgd.1c01227.

XRD θ–2θ scans, Raman spectra, deposition parameters, and fitted imaginary permittivity of the 20 and 120 nm films (PDF)

■ AUTHOR INFORMATION

Corresponding Author

Haiyan Wang − *School of Materials Engineering, Purdue University, West Lafayette, Indiana 47907, United States; School of Electrical and Computer Engineering, Purdue University, West Lafayette, Indiana 47907, United States;* orcid.org/0000-0002-7397-1209; Email: hwang00@purdue.edu

Authors

Juncheng Liu − *School of Materials Engineering, Purdue University, West Lafayette, Indiana 47907, United States*

Xuejing Wang − *School of Materials Engineering, Purdue University, West Lafayette, Indiana 47907, United States*

Xingyao Gao − *School of Materials Engineering, Purdue University, West Lafayette, Indiana 47907, United States*

Han Wang − *School of Materials Engineering, Purdue University, West Lafayette, Indiana 47907, United States*

Bruce Zhang − *School of Electrical and Computer Engineering, Purdue University, West Lafayette, Indiana 47907, United States*

Di Zhang − *School of Materials Engineering, Purdue University, West Lafayette, Indiana 47907, United States*

Matias Kalaswad − *School of Electrical and Computer Engineering, Purdue University, West Lafayette, Indiana 47907, United States*

Jijie Huang − *School of Materials Engineering, Purdue University, West Lafayette, Indiana 47907, United States*

Complete contact information is available at: https://pubs.acs.org/10.1021/acs.cgd.1c01227

Notes

The authors declare no competing financial interest.

https://doi.org/10.1021/acs.cgd.1c01227
Cryst. Growth Des. 2022, 22, 718−725

■ ACKNOWLEDGMENTS

This work was supported by the U.S. Department of Energy, Office of Science, Basic Energy Sciences (DE-SC0020077). This paper describes objective technical results and analysis. Any subjective views or opinions that might be expressed in the paper do not necessarily represent the views of the U.S. Department of Energy or the United States Government. Matias Kalaswad, Xuejing Wang, and Haiyan Wang acknowledge the support from the U.S. National Science Foundation (DMR-1565822 and DMR-2016453) for the microscopy efforts.

■ REFERENCES

(1) Yamamoto, Y.; Harada, S.; Yamamoto, D.; Honda, W.; Arie, T.; Akita, S.; Takei, K. Printed multifunctional flexible device with an integrated motion sensor for health care monitoring. *Sci. Adv.* **2016**, *2*, No. e1601473.

(2) Rogers, J. A.; Someya, T.; Huang, Y. Materials and mechanics for stretchable electronics. *Science* **2010**, *327*, 1603−1607.

(3) Bao, Z.; Chen, X. Flexible and Stretchable Devices. *Adv. Mater.* **2016**, *28*, 4177−4179.

(4) Gao, W.; Emaminejad, S.; Nyein, H. Y. Y.; Challa, S.; Chen, K.; Peck, A.; Fahad, H. M.; Ota, H.; Shiraki, H.; Kiriya, D.; Lien, D. H.; et al. Fully integrated wearable sensor arrays for multiplexed in situ perspiration analysis. *Nature* **2016**, *529*, 509−514.

(5) Son, D.; Lee, J.; Qiao, S.; Ghaffari, R.; Kim, J.; Lee, J. E.; Song, C.; Kim, S. J.; Lee, D. J.; Jun, S. W.; Yang, S.; et al. Multifunctional wearable devices for diagnosis and therapy of movement disorders. *Nat. Nanotechnol.* **2014**, *9*, 397−404.

(6) Gustafsson, G.; Cao, Y.; Treacy, G. M.; Klavetter, F.; Colaneri, N.; Heeger, A. J. Flexible light-emitting diodes made from soluble conducting polymers. *Nature* **1992**, *357*, 477−479.

(7) Cheung, Y. F.; Li, K. H.; Choi, H. W. Flexible free-standing III-nitride thin films for emitters and displays. *ACS Appl. Mater. Interfaces* **2016**, *8*, 21440−21445.

(8) Bauer, S.; Bauer-Gogonea, S.; Graz, I.; Kaltenbrunner, M.; Keplinger, C.; Schwödiauer, R. 25th Anniversary Article: A Soft Future: From Robots and Sensor Skin to Energy Harvesters. *Adv. Mater.* **2014**, *26*, 149−162.

(9) Kim, C. S.; Yang, H. M.; Lee, J.; Lee, G. S.; Choi, H.; Kim, Y. J.; Lim, S. H.; Cho, S. H.; Cho, B. J. Self-powered wearable electrocardiography using a wearable thermoelectric power generator. *ACS Energy Lett.* **2018**, *3*, 501−507.

(10) Wee, S. H.; Huang, P. S.; Lee, J. K.; Goyal, A. Heteroepitaxial Cu_2O thin film solar cell on metallic substrates. *Sci. Rep.* **2015**, *5*, No. 16272.

(11) Dutta, P.; Rathi, M.; Zheng, N.; Gao, Y.; Yao, Y.; Martinez, J.; Ahrenkiel, P.; Selvamanickam, V. High mobility single-crystalline-like GaAs thin films on inexpensive flexible metal substrates by metal-organic chemical vapor deposition. *Appl. Phys. Lett.* **2014**, *105*, No. 092104.

(12) Huang, J.; Chen, L.; Jian, J.; Khatkhatay, F.; Jacob, C.; Wang, H. A simplified superconducting coated conductor design with Fe-based superconductors on glass and flexible metallic substrates. *J. Alloys Compd.* **2015**, *647*, 380−385.

(13) Barlow, S. G.; Manning, D. A. C. Influence of time and temperature on reactions and transformations of muscovite mica. *Br. Ceram. Trans.* **1999**, *98*, 122−126.

(14) Bitla, Y.; Chu, Y. H. MICAtronics: A new platform for flexible X-tronics. *FlatChem* **2017**, *3*, 26−42.

(15) Liu, H. J.; Wang, C. K.; Su, D.; Amrillah, T.; Hsieh, Y. H.; Wu, K. H.; Chen, Y. C.; Juang, J. Y.; Eng, L. M.; Jen, S. U.; Chu, Y. H. Flexible heteroepitaxy of $CoFe_2O_4$/muscovite bimorph with large magnetostriction. *ACS Appl. Mater. Interfaces* **2017**, *9*, 7297−7304.

(16) Huang, J.; Wang, H.; Sun, X.; Zhang, X.; Wang, H. Multifunctional $La_{0.67}Sr_{0.33}MnO_3$ (LSMO) thin films integrated on mica substrates toward flexible spintronics and electronics. *ACS Appl. Mater. Interfaces* **2018**, *10*, 42698−42705.

(17) Li, C. I.; Lin, J. C.; Liu, H. J.; Chu, M. W.; Chen, H. W.; Ma, C. H.; Tsai, C. Y.; Huang, H. W.; Lin, H. J.; Liu, H. L.; Chiu, P. W.; et al. Van der Waal epitaxy of flexible and transparent VO_2 film on muscovite. *Chem. Mater.* **2016**, *28*, 3914−3919.

(18) Ma, C. H.; Lin, J. C.; Liu, H. J.; Do, T. H.; Zhu, Y. M.; Ha, T. D.; Zhan, Q.; Juang, J. Y.; He, Q.; Arenholz, E.; Chiu, P. W.; et al. Van der Waals epitaxy of functional MoO_2 film on mica for flexible electronics. *Appl. Phys. Lett.* **2016**, *108*, No. 253104.

(19) Amrillah, T.; Bitla, Y.; Shin, K.; Yang, T.; Hsieh, Y. H.; Chiou, Y. Y.; Liu, H. J.; Do, T. H.; Su, D.; Chen, Y. C.; Jen, S. U.; et al. Flexible multiferroic bulk heterojunction with giant magnetoelectric coupling via van der Waals epitaxy. *ACS Nano* **2017**, *11*, 6122−6130.

(20) Liu, J.; Wang, X.; Gao, X.; Wang, H.; Jian, J.; Huang, J.; Sun, X.; Qi, Z.; Misra, S.; He, Z.; Wang, H. Multifunctional self-assembled $BaTiO_3$-Au nanocomposite thin films on flexible mica substrates with tunable optical properties. *Appl. Mater. Today* **2020**, *21*, No. 100856.

(21) Huang, J.; Wang, H.; Wang, X.; Gao, X.; Liu, J.; Wang, H. Exchange Bias in a $La_{0.67}Sr_{0.33}MnO_3$/NiO Heterointerface Integrated on a Flexible Mica Substrate. *ACS Appl. Mater. Interfaces* **2020**, *12*, 39920−39925.

(22) Kim, H.; Kim, Y.; Kim, K. S.; Jeong, H. Y.; Jang, A. R.; Han, S. H.; Yoon, D. H.; Suh, K. S.; Shin, H. S.; Kim, T.; Yang, W. S. Flexible thermochromic window based on hybridized VO_2/graphene. *ACS Nano* **2013**, *7*, 5769−5776.

(23) Zhang, W.; Ramesh, R.; MacManus-Driscoll, J. L.; Wang, H. Multifunctional, self-assembled oxide nanocomposite thin films and devices. *MRS Bull.* **2015**, *40*, 736−745.

(24) Lebedev, O. I.; Verbeeck, J.; Van Tendeloo, G.; Shapoval, O.; Belenchuk, A.; Moshnyaga, V.; Damashcke, B.; Samwer, K. Structural phase transitions and stress accommodation in $(La_{0.67}Ca_{0.33}MnO_3)_{1-x}$:$(MgO)_x$ composite films. *Phys. Rev. B* **2002**, *66*, No. 104421.

(25) Zheng, H.; Wang, J.; Lofland, S. E.; Ma, Z.; Mohaddes-Ardabili, L.; Zhao, T.; Salamanca-Riba, L.; Shinde, S. R.; Ogale, S. B.; Bai, F.; Viehland, D.; et al. Multiferroic $BaTiO_3$-$CoFe_2O_4$ nanostructures. *Science* **2004**, *303*, 661−663.

(26) MacManus-Driscoll, J. L.; Zerrer, P.; Wang, H.; Yang, H.; Yoon, J.; Fouchet, A.; Yu, R.; Blamire, M. G.; Jia, Q. Strain control and spontaneous phase ordering in vertical nanocomposite heteroepitaxial thin films. *Nat. Mater.* **2008**, *7*, 314−320.

(27) Chen, A.; Bi, Z.; Hazariwala, H.; Zhang, X.; Su, Q.; Chen, L.; Jia, Q.; MacManus-Driscoll, J. L.; Wang, H. Microstructure, magnetic, and low-field magnetotransport properties of self-assembled $(La_{0.7}Sr_{0.3}MnO_3)_{0.5}$:$(CeO_2)_{0.5}$ vertically aligned nanocomposite thin films. *Nanotechnology* **2011**, *22*, No. 315712.

(28) Li, L.; Misra, S.; Gao, X.; Liu, J.; Wang, H.; Huang, J.; Zhang, B.; Lu, P.; Wang, H. Novel vertically aligned nanocomposite of Bi_2WO_6-Co_3O_4 with room-temperature multiferroic and anisotropic optical response. *Nano Res.* **2021**, *14*, 4789−4794.

(29) Li, L.; Sun, L.; Gomez-Diaz, J. S.; Hogan, N. L.; Lu, P.; Khatkhatay, F.; Zhang, W.; Jian, J.; Huang, J.; Su, Q.; Fan, M.; et al. Self-assembled epitaxial Au−Oxide vertically aligned nanocomposites for nanoscale metamaterials. *Nano Lett.* **2016**, *16*, 3936−3943.

(30) Huang, J.; Li, L.; Lu, P.; Qi, Z.; Sun, X.; Zhang, X.; Wang, H. Self-assembled Co−$BaZrO_3$ nanocomposite thin films with ultra-fine vertically aligned Co nanopillars. *Nanoscale* **2017**, *9*, 7970−7976.

(31) Huang, J.; Qi, Z.; Li, L.; Wang, H.; Xue, S.; Zhang, B.; Zhang, X.; Wang, H. Self-assembled vertically aligned Ni nanopillars in CeO_2 with anisotropic magnetic and transport properties for energy applications. *Nanoscale* **2018**, *10*, 17182−17188.

(32) Wang, X.; Choi, J.; Liu, J.; Malis, O.; Li, X.; Bermel, P.; Zhang, X.; Wang, H. 3D Hybrid Trilayer Heterostructure: Tunable Au Nanorods and Optical Properties. *ACS Appl. Mater. Interfaces* **2020**, *12*, 45015−45022.

(33) Wang, X.; Qi, Z.; Liu, J.; Wang, H.; Xu, X.; Zhang, X.; Wang, H. Strong Interfacial Coupling of Tunable Ni−NiO Nanocomposite Thin Films Formed by Self-Decomposition. *ACS Appl. Mater. Interfaces* **2021**, *13*, 39730−39737.

https://doi.org/10.1021/acs.cgd.1c01227
Cryst. Growth Des. 2022, 22, 718−725

(34) Zhang, B.; Huang, J.; Jian, J.; Rutherford, B. X.; Li, L.; Misra, S.; Sun, X.; Wang, H. Tuning magnetic anisotropy in Co−$BaZrO_3$ vertically aligned nanocomposites for memory device integration. *Nanoscale Adv.* **2019**, *1*, 4450−4458.
(35) Zhang, B.; Huang, J.; Rutherford, B. X.; Lu, P.; Misra, S.; Kalaswad, M.; He, Z.; Gao, X.; Sun, X.; Li, L.; Wang, H. Tunable, room-temperature multiferroic Fe-$BaTiO_3$ vertically aligned nanocomposites with perpendicular magnetic anisotropy. *Mater. Today Nano* **2020**, *11*, No. 100083.
(36) Paldi, R. L.; Sun, X.; Wang, X.; Zhang, X.; Wang, H. Strain-Driven In-plane Ordering in Vertically Aligned ZnO−Au Nanocomposites with Highly Correlated Metamaterial Properties. *ACS Omega* **2020**, *5*, 2234−2241.
(37) Zhang, D.; Misra, S.; Li, L.; Wang, X.; Jian, J.; Lu, P.; Gao, X.; Sun, X.; Qi, Z.; Kalaswad, M.; Zhang, X.; et al. Tunable Optical Properties in Self-Assembled Oxide-Metal Hybrid Thin Films via Au-Phase Geometry Control: From Nanopillars to Nanodisks. *Adv. Opt. Mater.* **2020**, *8*, No. 1901359.
(38) Zhang, D.; Lu, P.; Misra, S.; Wissel, A.; He, Z.; Qi, Z.; Gao, X.; Sun, X.; Liu, J.; Lu, J.; Zhang, X. Design of 3D Oxide−Metal Hybrid Metamaterial for Tailorable Light−Matter Interactions in Visible and Near-Infrared Region. *Adv. Opt. Mater.* **2021**, *9*, No. 2001154.
(39) Diao, Z.; Li, Z.; Wang, S.; Ding, Y.; Panchula, A.; Chen, E.; Wang, L. C.; Huai, Y. Spin-transfer torque switching in magnetic tunnel junctions and spin-transfer torque random access memory. *J. Phys.: Condens. Matter* **2007**, *19*, No. 165209.
(40) Nishimura, N.; Hirai, T.; Koganei, A.; Ikeda, T.; Okano, K.; Sekiguchi, Y.; Osada, Y. Magnetic tunnel junction device with perpendicular magnetization films for high-density magnetic random access memory. *J. Appl. Phys.* **2002**, *91*, 5246−5249.
(41) Chun, K. C.; Zhao, H.; Harms, J. D.; Kim, T. H.; Wang, J. P.; Kim, C. H. A scaling roadmap and performance evaluation of in-plane and perpendicular MTJ based STT-MRAMs for high-density cache memory. *IEEE J. Solid-State Circuits* **2013**, *48*, 598−610.
(42) Baillet, S. Magnetoencephalography for brain electrophysiology and imaging. *Nat. Neurosci.* **2017**, *20*, 327−339.
(43) Kaka, S.; Pufall, M. R.; Rippard, W. H.; Silva, T. J.; Russek, S. E.; Katine, J. A. Mutual phase-locking of microwave spin torque nano-oscillators. *Nature* **2005**, *437*, 389−392.
(44) Kiselev, S. I.; Sankey, J. C.; Krivorotov, I. N.; Emley, N. C.; Schoelkopf, R. J.; Buhrman, R. A.; Ralph, D. C. Microwave oscillations of a nanomagnet driven by a spin-polarized current. *Nature* **2003**, *425*, 380−383.
(45) Slonczewski, J. C. Current-driven excitation of magnetic multilayers. *J. Magn. Magn. Mater.* **1996**, *159*, L1−L7.
(46) Kalaswad, M.; Zhang, B.; Wang, X.; Wang, H.; Gao, X.; Wang, H. Integration of highly anisotropic multiferroic $BaTiO_3$−Fe nanocomposite thin films on Si towards device applications. *Nanoscale Adv.* **2020**, *2*, 4172−4178.
(47) Xu, R.; Zhang, X.; Zhang, D.; Liu, J.; Lu, J.; Zhao, R.; Ji, Y.; Qian, F.; Wang, H.; Fan, J.; Li, W. High stability of flexible perovskite transparent conductive oxide film via van der Waals heteroepitaxy. *J. Alloys Compd.* **2021**, *890*, No. 161897.
(48) Radtke, G.; Hennes, M.; Bugnet, M.; Ramasse, Q. M.; Weng, X.; Demaille, D.; Gobaut, B.; Ohresser, P.; Otero, E.; Choueikani, F.; Juhin, A.; et al. Atomic-Scale Study of Metal−Oxide Interfaces and Magnetoelastic Coupling in Self-Assembled Epitaxial Vertically Aligned Magnetic Nanocomposites. *Adv. Mater. Interfaces* **2019**, *6*, No. 1900549.
(49) Zhang, D.; Misra, S.; Jian, J.; Lu, P.; Li, L.; Wissel, A.; Zhang, X.; Wang, H. Self-Assembled $BaTiO_3$−Au_xAg_{1-x} Low-Loss Hybrid Plasmonic Metamaterials with an Ordered "Nano-Domino-like" Microstructure. *ACS Appl. Mater. Interfaces* **2021**, *13*, 5390−5398.

https://doi.org/10.1021/acs.cgd.1c01227
Cryst. Growth Des. 2022, 22, 718−725